Embedding atomic cobalt within hierarchical porous carbon derived from cross-linked polymers for high energy supercapacitors

Daba T. Bakhoum [a], Samba Sarr [a], Vusani M. Maphiri [a], Ndeye F. Sylla [a], Ndeye M. Ndiaye [b], Modou Diop [c], Balla D. Ngom [b], Mohamed Chaker [c] and Ncholu Manyala [a*]

[a] Department of Physics, University of Pretoria, Pretoria 0028, South Africa

[b] Laboratoire de Photonique Quantique, d'Energie et de Nano-Fabrication, Faculté des Sciences et Techniques Université Cheikh Anta Diop de Dakar (UCAD) B.P. 5005 Dakar-Fann Dakar, Sénégal

[c] Institut National de la Recherche Scientifique Centre-Énergie Matériaux Télécommunications 1650, Boulevard Lionel Boulet, Varennes, QC J3X 1S2, Canada

*Corresponding author's email: ncholu.manyala@up.ac.za, Tel.: + (27)12 420 3549, Fax: + (27)12 420 2516

Abstract

In this study, we have described a straightforward and useful method for synthesizing activated carbon doped with cobalt from cross-linked polymers (Polyvinyl alcohol and Polyvinyl pyrrolidone) with good electrochemical performance. In fact, cobalt (Co) was directly incorporated in the polymers through hydrothermal by varying the amount (0.5% w/v; 1% w/v and 2% w/v) of cobalt precursor ($Co(NO_3)_2 \cdot 6H_2O$) in the Polyvinyl alcohol (PVA) and Polyvinylpyrrolidone (PVP) polymers' solution. The cobalt doped porous carbon shown good features bestowing to the porous structure, metal doping and high conductivity. These characteristics result in more active sites, stored charges, and assistance with the quick passage of electrolytes ions into the porous carbon electrode. At a specific current of 0.5 A g^{-1}, an assembled symmetric supercapacitor AC-PVA/PVP/Co-1//AC-PVA/PVP/Co-1 supply a significant amount of specific energy and power of 32 W h kg^{-1} and 401 W kg^{-1}, respectively. For the symmetric cell, a stability of 91% up to 10,000 cycles was noted. So, the optimized AC-PVA/PVP/Co has a lot of potential for real-world supercapacitor applications.

Keywords: Polymers; energy storage; cobalt-doping; specific energy; supercapacitor

1. Introduction

Supercapacitors (SCs) are an efficient and sustainable energy storage device which bridges the gap between batteries and capacitors. SCs are devices with high specific power, fast charge/discharge ability, long lifespan and reliable safety [1]. However, their commercial applications have a major hurdle which is their low specific energy. In order to increase the specific energy, new efficient electrode materials have been synthesized such as heteroatom doped materials [2][3], metal and metal oxide doped materials [4][5] and composite materials [6][7]. Several authors have reported different routes to improve the electrochemical performance via the incorporation of the heteroatoms such as nitrogen (N), phosphorous (P), sulfur (S) and, boron (B) in the carbon matrix [8][9][10][11]. Recently, the effect of the N, P co-doping on porous carbon (AC) prepared from (PVA/PVP) cross-linked polymers was investigated. This study revealed that the co-doped sample AC-PVA/PVP/AP displayed higher electrochemical performance i.e. a specific capacitance of 252 F g^{-1} which is 67.5 % increase from the undoped AC-PVA/PVP (170 F g^{-1}) [12] .

Modifying the features of the porous carbon by incorporating metal or metal oxide such as cobalt (Co), iron (Fe), vanadium oxide (VO_2)) can also enhance the electrochemical properties. Reports have indicated that the metal/metal oxide doped porous carbon material has excellent electrical conductivities, good chemical stabilities and improved surface interfaces and redox activity [13]. Li et al. [14] have synthesized an iron doped biomass-based porous carbon using the carbonisation of the squid pen under nitrogen gas at 300 °C followed by an activation at 800 °C by varying the amount of ferric chloride ($FeCl_3$). They demonstrated that the iron doping improved the pseudocapacitance effect of the material and have an impact on the electrochemical performance of the porous carbon. The doped carbon displayed a specific capacitance of 131.7 F g^{-1} compared to 31.8 F g^{-1} for the undoped sample, at 0.2 A g^{-1}.

Ramakrishnan et al. [15] reported a straightforward procedure for embedding cobalt metal doped into the porous carbon nanorods (Co-CNRs). They have shown that cobalt doping creates active pores for electrolyte ions pathway and improve the conductivity (from 0.12 to 17 S m^{-1}) of the carbon material. The high conductive behaviour was also determined by using the electrochemical impedance spectroscopy (EIS) which shows smaller resistance of the doped material compared to the pristine sample. The specific capacitance was found to increase from 2 to 88 F g^{-1} at a current of 0.5 mA for the pristine and the doped sample respectively. The increase in performance of the doped carbon is due to the synergy between the electrical conductivity, the high porosity and specific surface area (SSA).

By fabricating cobalt-doped porous activated carbon from hyper crosslinked polymer with 5,10,15,20-Tetra (4-pyridyl) porphyrin as monomer, Chen et al. [16] have demonstrated that the symmetric cell exhibited a specific energy of 18.43 W h kg^{-1} corresponding to a specific power of 135 W kg^{-1}. The capacitance of the undoped (GPC) and the doped (cobalt-doped graphene-coupled porous carbon (Co-GPC) were found to be 244 F g^{-1} and 455 F g^{-1} at a specific current of 0.5 A g^{-1}, respectively. Their study revealed that the incorporation of cobalt into the carbon matrix increased the sample's conductivity while also giving it high pseudocapacitor property. Indeed, porous carbon materials possess a several advantages including excellent porosity, good electrical conductivity, great chemical and thermal stability. But in order to improve further its electrochemical properties, combining the merits of the pseudocapacitor such as cobalt doping with the porous carbon derived cross-linked polymers, is more beneficial for supercapacitor device.

Herein, we report the synthesis of Co-doped activated carbon from PVA/PVP cross-linked polymers by varying amount of cobalt precursor ratio to PVA/PVP (AC-PVA/PVP/Co-x) where x= 0.5 w%/v; 1 w%/v; 2 w%/v by hydrothermal method followed by one step activation. AC-PVA/PVP/Co-1 displays better capacitance than the undoped AC-PVA/PVP and the other doped carbons AC-PVA/PVP/Co-0.5 and, AC-PVA/PVP/Co-2. AC-PVA/PVP/Co-1 delivers the best energy storing capability as compared to all synthesized materials, leading to its use as electrode material for the symmetric device. The enhanced performance of the Co-doped carbon is due to the additional pseudocapacitance sites, and the improved conductivity brought by the cobalt metal. The AC-PVA/PVP/Co-1//AC-PVA/PVP/Co-1'energy storage performance was enhanced synergistically by correct amount of Co into the activated carbon matrix leading to high specific energy of 32 Wh kg^{-1} with a high specific power of 401 W kg^{-1} at 0.5 A g^{-1}.

2. Experimental section

2.1. Sample preparation

In this work, samples were synthesized similarly to our previously published work [17]. A yellowish powder was prepared by dissolving 10 g of PVA (semicrystalline and highly hydrophilic polymer, with many hydroxyls group), 2.5 g of PVP (vinyl synthetic amorphous polymer, very good solubility in water and many organic solvents) and varied amounts (0.5, 1 and 2 g) of cobalt nitrate hexahydrate ($Co(NO)_3)_2$•$6H_2O$) in 100 mL deionized (DI) water; and stirring the solution at constant heat of 80 °C for 2 h until a viscous homogeneous gel was formed. Thereafter, the gel was poured into a Teflon lined autoclave and subsequently heated in an electric oven at 180 °C for 14 h, as displayed in scheme 1. The obtained material was washed and rinsed with DI to remove all the possibility contaminations, then dried in a 60 °C electric oven for 12 h. The dried yellow powder was then activated by mixing it with potassium hydroxide at mass ratio of 1:2. The solid mixture was then heated for 2 h at 700 °C in argon gas atmosphere (300 sccm at 5 °C min^{-1}). Finally, the samples were collected and dried at 60 °C for 6 h after vigorous washing and rinsing with DI water repeatedly. Note that the samples were denoted as AC-PVA/PVP/Co-x, with x signifying the amount of cobalt precursor (i.e. x

= 0.5, 1 and 2 g) added during the sample preparation 100 mL of DI water and hence x can be donated as 0.5 wt%/v, 1 wt%/v and 2%w/v. The sample without cobalt is denoted as AC-PVA/PVP.

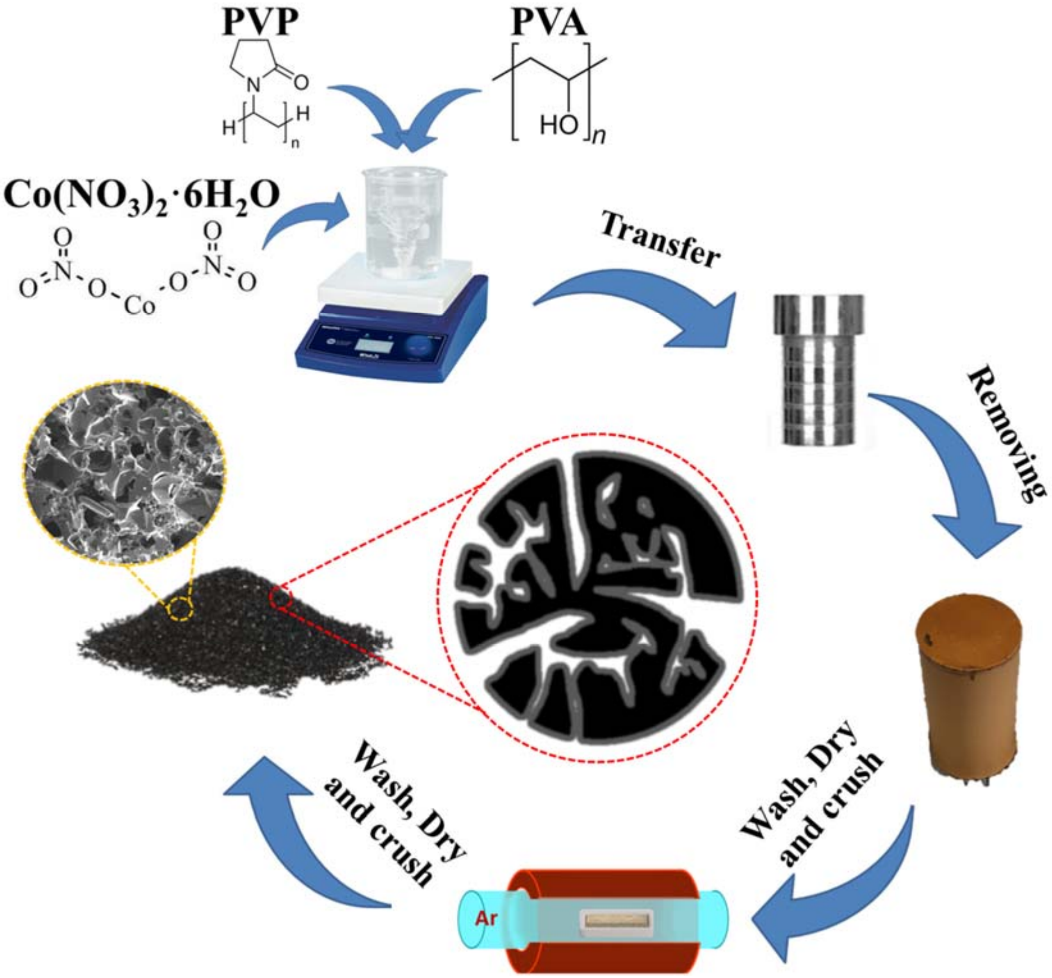

Scheme 1. Synthesis process of AC-PVA/PVP/Co-x.

2.2 Material characterization

The XRD-Bruker D8 Advance (Panalytical, Netherlands), with reflection geometry at 2θ values (10–90°) with a step size of 0.05° working with a CuK_α radiation source (λ = 0.1542 nm), together with micro-Raman (WITec alpha 300 RAS+ Confocal microscope (Focus Innovations, Ulm, Germany)) operated with a 532 nm laser wavelength at a laser power of 2mW were adopted for structural analysis. The morphological analysis was performed by a high-resolution Zeiss Ultra plus 55 field emission scanning electron microscope (FE-SEM) (Akishima-shi, Japan) operated at an accelerating voltage of 2.0 kV, while the chemical mapping analysis were performed by the Oxford X-Max 80 mm^2 energy dispersive X-ray spectroscopy (EDS) detector operated at an accelerating voltage of 20.0 kV coupled in FE-SEM and a VG Escalab 220i-XL X-ray photoelectron spectroscopy (Fisons instrument, UK) with a monochromatic Al- K_α (0.6 eV) source. Brunauer-Emmett-Teller (BET) method was employed to determine the specific surface area. The pore size distribution and the pore volume were obtained via the density functional theory (DFT) method. NOVA touch NT 2LX-1, Volts, USA coupled with quantachrome TouchWin software Version: 1.22 was used for all N_2 adsorption/desorption measurements at 77 K.

2.3 Electrochemical characterization

In summary, a slurry (total mass of 12 mg) was prepared by mixing 80 % (9.6 mg) of the prepared material with 10 % (1.2 mg) of acetylene carbon black (as a conductive material) and 10 % (1.2 mg) polyvinylidene fluoride (PVDF; as a binder) with few drops of N-methyl-2-pyrrolidone (NMP; as a solvent). Then coated onto a nickel foam current collector and dried in an electric oven for 6 h at 60 °C. The latter was then used as a working electrode, while saturated silver-silver chloride (Ag/AgCl) and glassy carbon were selected as reference and counter electrode in three-electrode system, respectively. A split cell was used in symmetric two-electrode measurement. The total mass per unit area of active material in the symmetric cell was calculated around 4.2 mg cm^{-2} while specific mass of 2.2 mg cm^{-2} was used in three-electrode set-up. Cyclic voltammetry (CV) and galvanostatic charge-discharge (GCD) curves were conducted at scan rates varying from 10 to 100 mV s^{-1} and a constant specific current of 0.5 to 10 A g^{-1}, respectively. The stability test was conducted using the GCD cycling test (cycling stability) and the floating test (voltage holding test). The GCD cycling consists of subjecting the device to a continuous charge discharge over 10,000 cycles at constant specific current of 5 A g^{-1}. For the floating test, three cycles were applied and then the device was hold at a maximum voltage of 1.6 V with a specific current of 5 A g^{-1} for 10 h. By occasional cycling the specific capacitance was determined, and the process is repeated for 190 h. Electrochemical impedance spectroscopy (EIS) analysis was performed at open circuit voltage over a frequency range from 100 kHz to 10 mHz. All electrochemical measurements were conducted at room temperature by using an electrochemical workstation (Bio-Logic VMP300 potentiostat (Knoxville TN, USA) with EC-Lab VI.41 software) in 2.5 M KNO_3 electrolyte.

3.Results and discussion

3.1. Morphological, textural and structural characterization

The X-ray diffraction (XRD) patterns of all AC-PVA/PVP/Co-x samples are displayed in Fig. S1 (supplementary information). The patterns display the presence of two prominent broad diffraction peaks at 19.3° and 43.7°, corresponding with the (002) and (101) crystallographic planes of carbon [18]. The broadness of these peaks suggest that the materials are amorphous carbons. The intensity of the (002) peak suggests that the AC-PVA/PVP/Co-1 has a high amorphous phase compared to the other prepared materials [19]. Moreover, a low diffraction peak shift was observed indicating the incorporation of a highly dispersed cobalt within the amorphous carbon matrix [20]. This is in accordance with the Vegard's law (although used in crystalline material) which suggest that the diffraction peak position shifts to lower diffraction angle when doped/incorporating ion (cobalt in this case) is bigger than the host element (carbon) [21][22]. Note that cobalt-based compounds were not observed due to the following reasons: Extremely low amounts of cobalt in the samples [15][23], incorporation of the cobalt in the carbon matrix [24] and the XRD instrument's detection limit [25][26].

To further investigate the structural vibrational properties of the synthesized materials, Raman measurements were carried out and displayed in Fig. 1. Like all other carbon-based materials, Raman spectra for all samples illustrate the presence of two peaks at 1345 cm^{-1} and 1580 cm^{-1} known as D and G bands. These bands are related to the defect and disordered carbon atoms and sp^2 hybridized carbon atoms, respectively [27]. The region between these two bands represents the presence of amorphous carbon (marked in blue line in Fig. 1 (a)), the absence of a pronounce notch corresponding to higher degree of amorphous carbon as seen in the XRD and thus AC-PVA/PVP/Co-1 has more amorphous carbon. The one phonon region vibration band of prepared samples were further analysed by Lorentz fitting with five peaks: I, D, D'', G, and D' attributed to the sp^2-sp^3 edge bonds, A_{1g} breathing mode, amorphous carbon, first-order Raman E_{2g} mode and disorder-induced phonon mode, respectively. The degree of defect (I_D/I_G) and amorphous ($I_{D''}/I_G$) were estimated from the areal ratio of the fitted peaks while the crystallite size (L_a) is determined using the knight equation (S1) and these values are displayed in table 1. It can be seen that the AC-PVA/PVP/Co-1 has the highest degree of defect, highest degree of amorphous carbon as can be seen on the XRD, which translate to low crystallite size due to cobalt ratio. This could enable more active sites and improved wettability, leading to better electrochemical behaviour [28][29] .

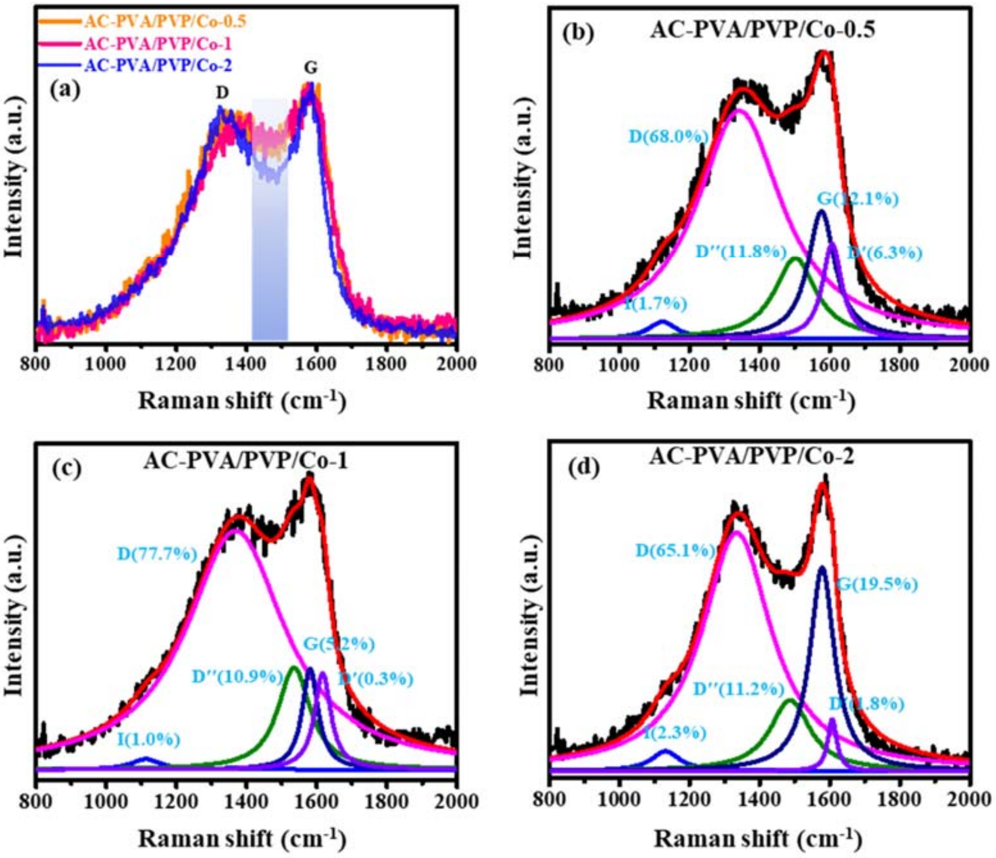

Fig. 1. (a) Raman spectra, and Lorentz fitted spectra of (b) AC-PVA/PVP/Co-0.5, (c) AC-PVA/PVP/Co-1 and (d) AC-PVA/PVP/Co-2 samples

Table 1. Samples and Raman calculated crystallite size (L_a), degree of defect (I_D/I_G) and degree of amorphous carbon ($I_{D''}/I_G$)

Samples	L_a (nm)	I_D/I_G	$I_{D''}/I_G$
AC-PVA/PVP/Co-0.5	0.8827	5.62	0.97
AC-PVA/PVP/Co-1	0.3296	15.05	2.12
AC-PVA/PVP/Co-2	1.4870	3.34	0.57

Nitrogen adsoprtion-desoprtion isotherms and pore size distribution of the prepared materials are displayed in Fig. 2 and the determined specific micropore area and specific surface area together with the corresponding total and micropore volume are summarized in Table. S1. From Fig. 2(a), all synthesized samples clearly display a well defined type I isotherm curve with a no obvious H4 hysteresis loop according to the IUPAC classification, which confirms the coexistence of the micropores and mesopores [30]. The calculated BET specific surface area (SSA) values of AC-PVA/PVP, AC-PVA/PVP/Co-0.5, AC-PVA/PVP/Co-1 and AC-PVA/PVP/Co-2 are 1680, 1645, 1591 and 1345 m^2 g^{-1}, respectively. It is obvious that AC-PVA/PVP has the highest SSA among all samples. After increasing the cobalt nitrate precursor loading from 0.5 to 2 g, the SSA was found to decrease. The total pore volume and the micropore volume followed the same trend (see table S1). The decrease of SSA might be due to the fact that the cobalt particles block some pores because of being incorporated in the carbon framework [31].

The pore size distribution plots from the DFT method of all the as-obtained samples are displayed in Fig. 2(b) and it confirms the coexistence of the micropores and mesopores. The micro-mesopore structures with high SSA and large pore volume can offer space for ions accommodations and easy transfer of the ions across the pores channels [32][30].

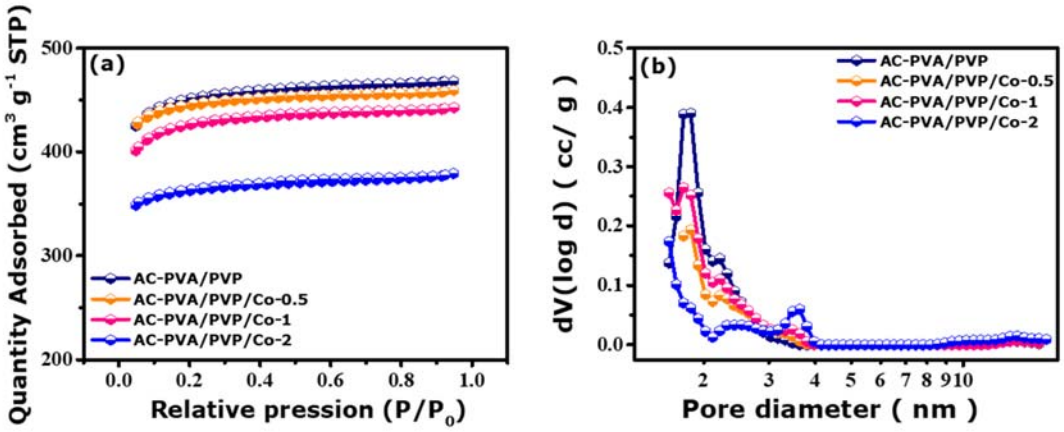

Fig. 2. (a) N_2 adsorption/desorption and (b) pore-size distribution of AC-PVA/PVP, AC-PVA/PVP/Co-x samples.

The surface morphology of all prepared carbons is shown in Fig. 3 and displays an interconnected cavity. The scanning electron microscopy (SEM) micrographs show a slightly rough surface with randomly distributed agglomerated nanoparticles due to the presence of cobalt within the carbon matrix. With the increase in the amount of cobalt, the nanoparticles get aggregated, and clusters of nanoparticles are observed [20][33]. With a high concentration of cobalt, the porous morphology of the AC-PVA/PVP/Co-2 sample shows an aggregation of particles blocking some pores on the surface, which is in perfect correlation with BET SSA. The interconnected channels facilitate the transport of the ions through the carbon matrix, increasing the ions-accessible surface area [34][35]. Among the cobalt-doped, AC-PVA/PVP/Co-1 displayed the greatest interconnected porous framework than other doped carbons. This might be due to the appropriate amount of cobalt dopant in the cross-linked polymers.

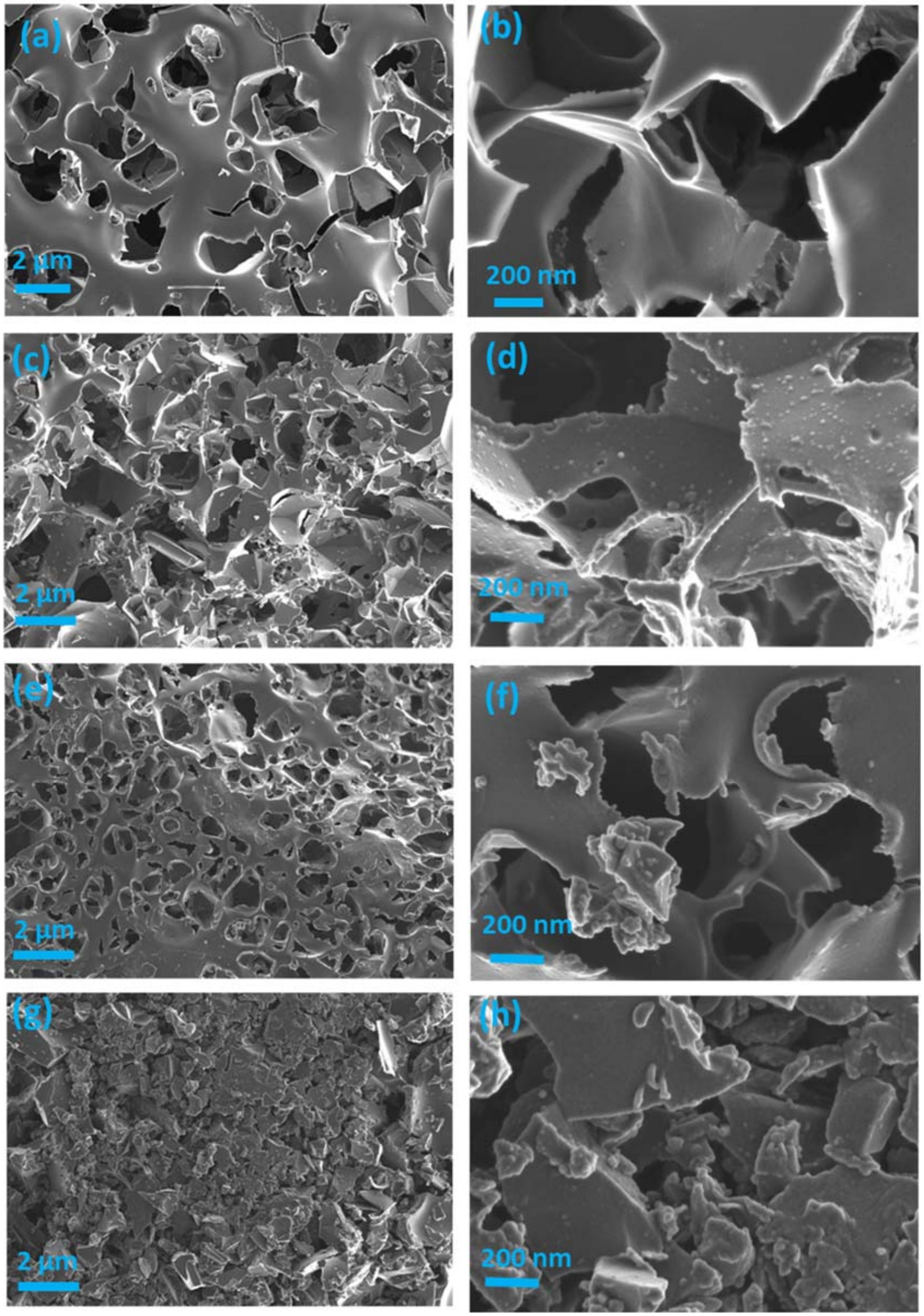

Fig. 3. SEM micrographs at low and high magnification of (a-b) AC-PVA/PVP, (c-d) AC-PVA/PVP/Co-0.5, (e-f) AC-PVA/PVP/Co-1 and (g-h) AC-PVA/PVP/Co-2 samples.

The elemental composition of the AC-PVA/PVP/Co-x samples was analysed by the energy dispersive X-ray spectroscopy EDS. The corresponding element mapping is shown in Fig. 4 which indicates the presence of uniform distribution of carbon, oxygen, nitrogen and cobalt in all samples.

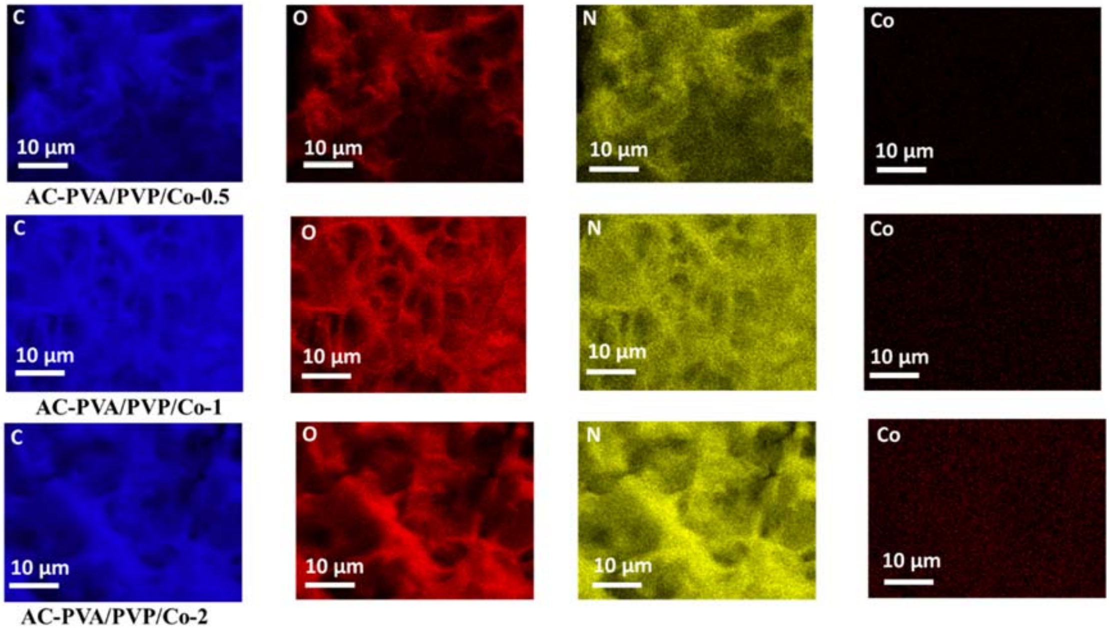

Fig. 4. EDS imaging micrographs of all doped samples

X-ray photoelectron spectroscopy (XPS) was conducted to assess the chemical composition and the electronic states of C, O, N and Co in AC-PVA/PVP/Co-x samples. Fig. S2 in the supporting information for AC-PVA/PVP/Co-2 reveal the presence of the four elements in the sample, which correlates with EDS mapping, further suggesting that Co was effectively incorporated into the carbon matrix. The survey displays four characteristic peaks around 284.6, 532.3, 400.4 and 785.4 eV attributed to C1s, O1s, N1s and Co2p, respectively [25][36]. C1s high-resolution XPS spectrum (Fig. 5(a)) shows four distinct peaks. The peaks at 284.5, 285.1, 286.4 and 288.2 eV are assigned to C-C/C=C, C-N, C-O and -C=O/O=C-, respectively [37][38]. Some studies reported that C-N can improve the conductivity and the activity of the sample by providing active sites [36][39]. O1s high-resolution XPS spectrum can be decomposed into four peaks as exhibited in Fig. 5(b). They correspond to 530.8, 531.8, 533.3 and 535.2, which are related to C-O/Co-O, -OH, C=O and O=C-OH, respectively [40]. The presence of Co^{2+} in Co-O can be assigned to the incomplete reduction of cobalt ions, or the partial oxidation of metallic cobalt surface in air [37][41]. N1s high-resolution spectrum (Fig. 5(c)) indicates the presence of N in the carbon with four peaks belonging to pyridinic N (398.7 eV), pyrrolic-N and Co-N (400.3 eV), graphitic-N (402 eV) and oxidized-N (403.4 eV) [42][25][43]. Pyridinic-N and graphitic-N are well-known for providing more active sites which can alter the activity and the stability of the material [44][36]. The presence of the N in the samples is due to the PVP, which is one of the cross-linking precursors and probably from the cobalt precursor. All these functional groups improve the structural defect and the electrochemical performance of the electrode material [41]. It was reported that the existence of N plays the role of the uniform dispersion of Co and signals the improvement of the interaction between the carbon and Co [41][45]. This is due to the nitrogen atoms' chemical activity and the ability to facilitate the direct attachment of metal precursors [46]. In addition, the Co-N and C-N groups enhance uniform dispersion of cobalt nanoparticles by forming a strong interfacial interaction between the core of cobalt nanoparticles and the N-doped carbon shell [47]. Co 2p3/2 and Co 2p1/2 peaks are detected around 782.5 and 797.6 eV, respectively as seen in Fig. 5(d), which match with metallic cobalt values [42][39][38][48]. Additionally, shoulder peaks at 789.5 and 804.5 eV are referred to as satellites and Co-N [42]. The satellite suggests Co-O due to the surface oxidation of Co [43][36][49]. Moreover, the cobalt 2p spectrum’s oscillating curve revealed the cobalt element’s low concentration [25]. Co enhances the conductivity of the electrode material and generates partially graphitized carbon which agrees with the Raman data [44]. Previous studies have established that Co-N and Co nanoparticles are suitable for the enhancement of the electrochemical performance [43][49]. It is rational to assume that the synergistic interactions between the Co-N, pyridinic-N and Co will lead to improved electrochemical performance of the Co-doped carbon [49].

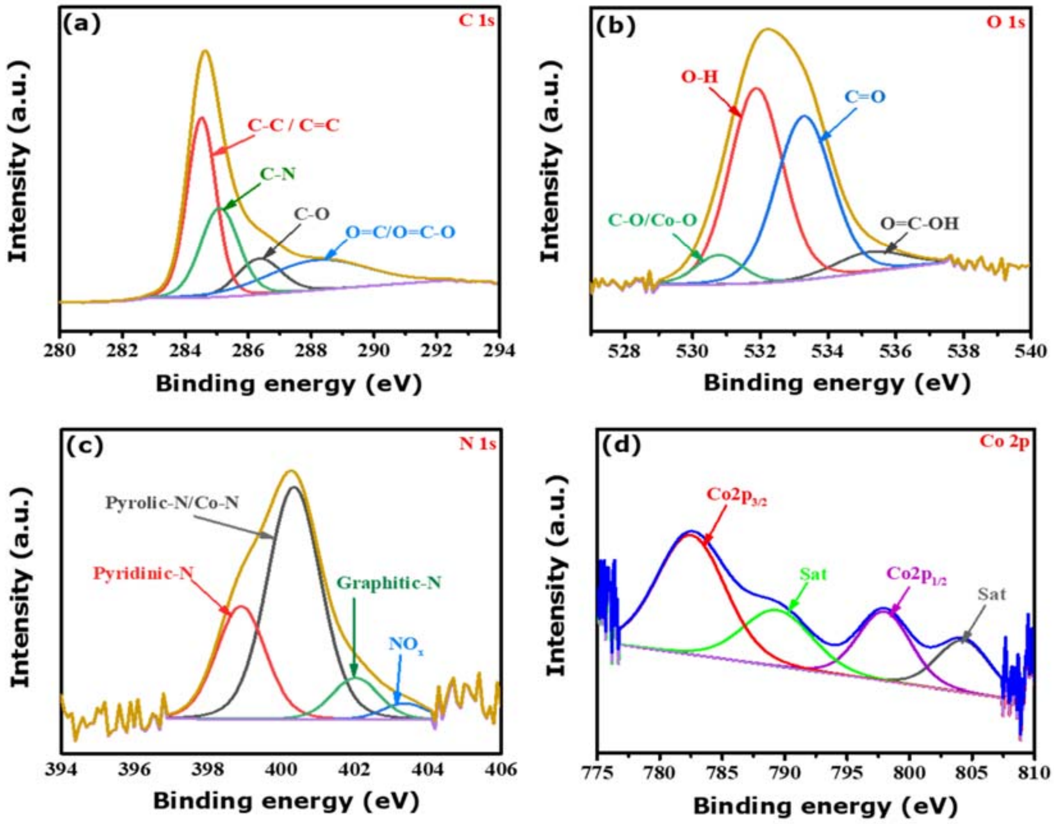

Fig. 5. XPS curves deconvoluted (a) C1s, (b) O1s, N1s and (d) Co2p of the prepared AC-PVA/PVP/Co-2.

3.2 Electrochemical analysis

3.2.1. Three-electrode evaluations

Three electrode measurements were carried out in 2.5M KNO$_3$ electrolyte, in order to analyse the electrochemical performance of the prepared materials. The cyclic voltammogram (CV) curves were performed in the negative and positive potential window ranging from -0.8 to 0V and 0 to 0.8V at a scan rate of 50 mV s^{-1} using saturated Ag/AgCl as reference (see Fig. 6 (a-b)). The CV plots show that all of the samples at various scan rate are depicted in Fig. S3 which illustrate typical rectangular shape which illustrates electric double layer capacitor (EDLC) behaviour. Nevertheless, no distinguishable redox peaks were seen in CV curves. It depicts the materials being charged and discharged in fast and reversible redox at a constant rate [20][50]. The current response in all cobalt-doped materials is greater than the AC-PVA/PVP, demonstrating the influence of Co doping on the electrochemical features due to the incorporation of the redox activity in the PVA/PVP cross-linked polymers. Among the doped carbon, AC-PVA/PVP/Co-1 displayed the higher current response, in both negative and positive potential which suggests the high specific capacitance. The galvanostatic charge-discharge (GCD) was used to analyse the charge-discharge storage capacity of the prepared samples as shown in Fig. 6(c-d). Similarly, to the CV curves, the GCD curves were performed in a negative and positive potential window range of -0.8 to 0V and 0 to 0.8V at a specific current of 1 A g^{-1}. All plots exhibited a quasi-symmetrical triangular shape confirming the reversible reaction between electrode and electrolyte and also confirming the capacitive feature as observed on the CV curves.

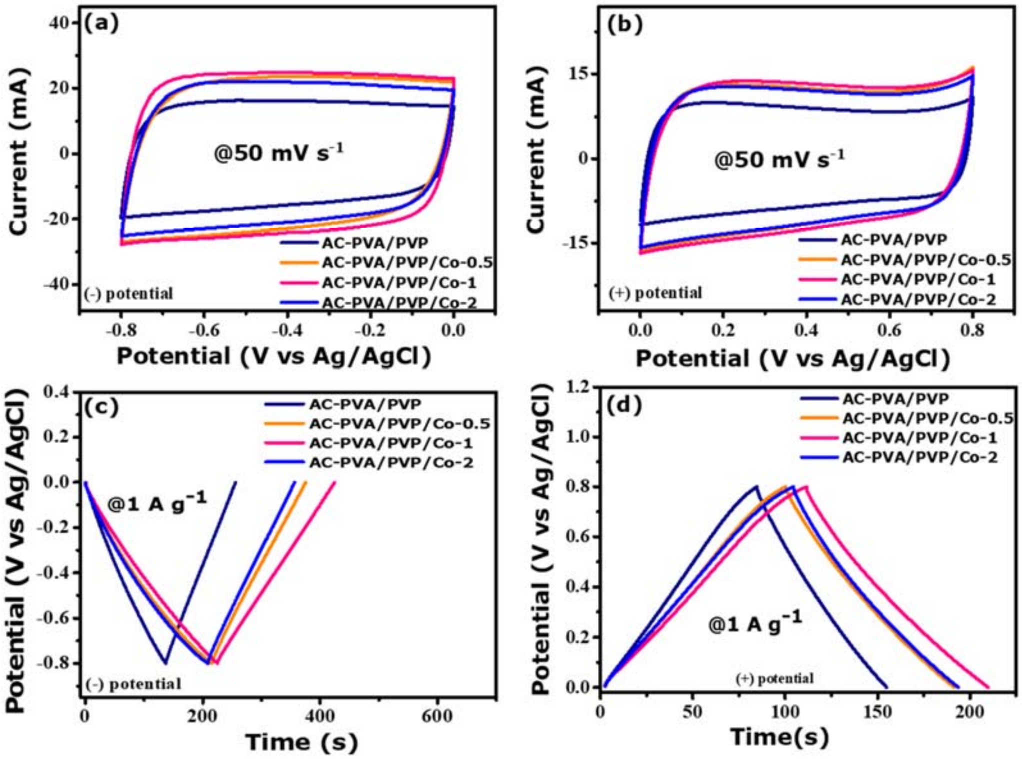

Fig. 6. (a-b) CV; and (c-d) GCD curves of prepared sample in negative and positive potentials.

A Trasatti analysis displayed on Fig. S4 was performed to calculate the pseudocapacitance and EDL capacitance contributions. The maximum total capacitance (C_T) was obtained from the reciprocal of the extrapolated intercept of the $1/C_T$ versus $\upsilon^{0.5}$ and the maximum EDL capacitance (C_{EDL}) was estimated from the extrapolated intercept of C_{EDL} versus $\upsilon^{-0.5}$. The maximum pseudocapacitance (C_{Pseudo}) was obtained from the difference between C_T and C_{EDL} using Eq. (S2), while the percentage contribution of C_{EDL} and C_{Pseudo} where calculated using Eqs. S4 and S5. The obtained values are displayed in Table S2 and Fig. 7(a). It can also be seen that the pseudocapacitive mechanism dominated as the cobalt content increases. Fig. 7(b-c) showed the calculated values of the specific capacitance for the prepared samples at different specific currents ranging from 1 to 10 A g^{-1}, using the GCD plots and equation S2. The estimated specific capacitances at 1 Ag^{-1} in both negative and positive potential are displayed in Table 2, and it is evident that indeed cobalt has significantly improved specific capacitance. AC-PVA/PVP/Co-1 exhibits the highest specific capacitance and a better residual capacitance at 10 A g^{-1}, this behaviour might be due to, a proper dopant content, porous structure from the SEM, highest degree of defect and amorphous carbon from Raman than the others doped carbon. In comparison to AC-PVA/PVP/Co-0.5 and AC-PVA/PVP/Co-1 which show a positive effect on Co-doping, the specific capacitance of AC-PVA/PVP/Co-2 was shown to be reducing. It is due to the fact that higher Co incorporation into the carbon matrix led to the destruction of the morphology as seen in the SEM image of Fig. 3 (g, h). It can also be due to the result of particles aggregation, which makes the AC-PVA/PVP/Co-2 sample bulky with clusters hindering the transport of the electrolyte ions in the material [20].

Table 2. Samples, specific capacitance (C_s), and residual capacitance in negative and positive potential

Samples	Negative potential		Positive potential	
	C_s at 1 Ag^{-1} (Fg^{-1})	Residual C_s at 10 Ag^{-1} (%)	C_s at 1 Ag^{-1} (Fg^{-1})	Residual C_s at 10 Ag^{-1} (%)
AC-PVA/PVP	170.3	78.68	88	79.66
AC-PVA/PVP/Co-0.5	271	71.59	107	79.44
AC-PVA/PVP/Co-1	280	76.79	123	72.36
AC-PVA/PVP/Co-2	261	65.90	111	70.27

The electrochemical impedance spectroscopy (EIS) was deployed to investigate the electrochemical behaviour, charge transfer kinetics and the impact of the doping on the internal resistance. The Nyquist plots with an inset displaying the values of the equivalent series resistance (ESR) for all activated carbon are shown in Fig. 7(d). A semicircle and a quasi-vertical line are visible at high and low-frequency regions, respectively. This is an indication of the presence of charge transfer resistance at the electrode/electrolyte interface and the capacitive behaviour of the electrodes. The Co-doped carbon presented a smaller ESR than the undoped AC-PVA/PVP (see Table S3) which indicates the effect of cobalt doping on the conductivity of the materials. The Nyquist plot also shows that the AC-PVA/PVP/Co-1 has the shortest diffusion length, with the slope closer to the Y-axis suggesting good capacitive behaviour as reported by Mathis et al [51]. The AC-PVA/PVP/Co-1 also shows the smallest ESR than other doped samples suggesting a good diffusion of electrolyte ions, more conductive pathways and great electrode/electrolyte interaction leading to the enhancement of the electrochemical performances [52].

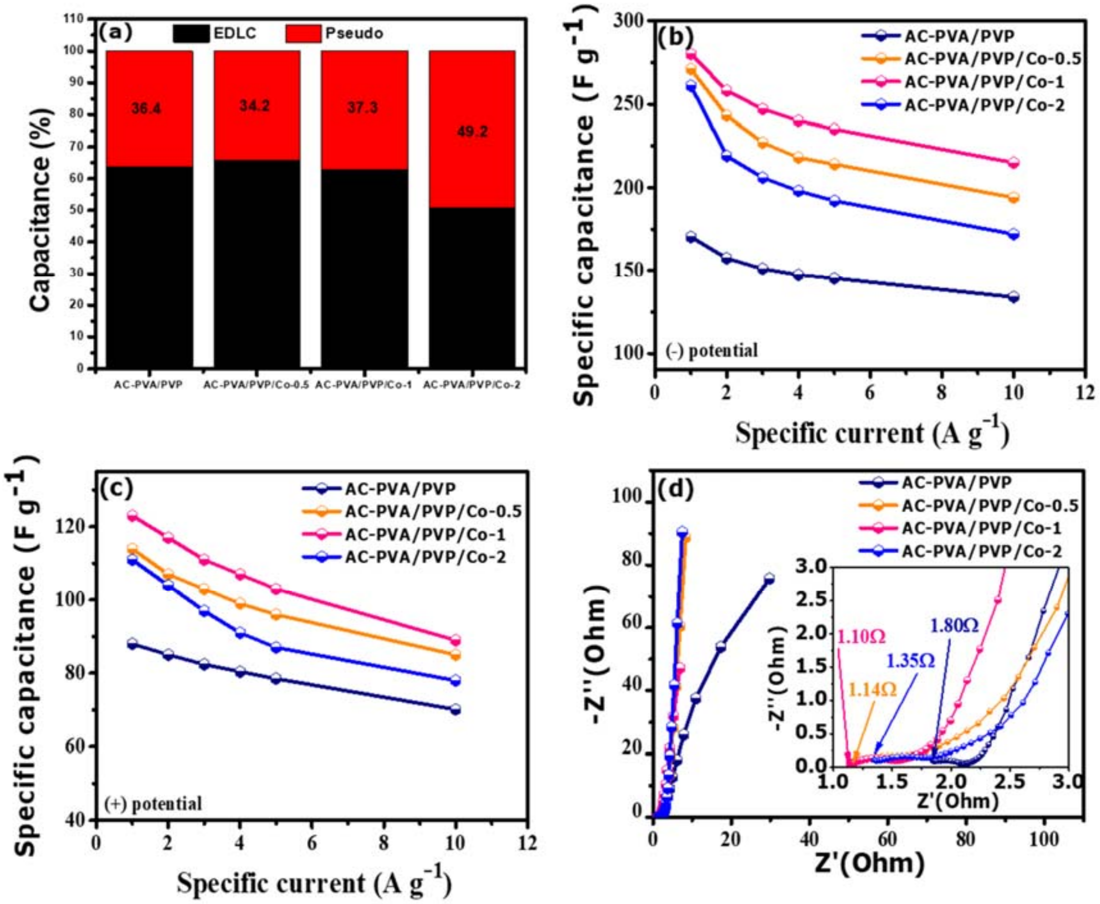

Fig. 7. (a) Trasatti's method calculated EDL and Pseudocapacitor contribution **(**c-d) specific capacitance versus specific current in both negative and positive potentials, respectively and (e) Nyquist impedance plots of the prepared materials.

3.2.2. Two electrode measurement

The best performing AC-PVA/PVP/Co-1 was selected and used to fabricate a symmetric supercapacitor device i.e. AC-PVA/PVP/Co-1//AC-PVA/PVP/Co-1 with 2.5 M KNO_3 aqueous electrolyte. Fig. 8(a) exhibits CV curves of the device that display a rectangular shape showing EDLC behaviour and the shape was also conserved at a high scan rate of 800 mV s^{-1} within the potential window of 1.6 V suggesting good charge propagation and fast ionic transport [53]. Fig. 8 (b) shows the GCD of the device measured at various specific currents ranging from 0.5 to 10 A g^{-1} and also confirms the EDLC behaviour seen in the CV curves. The specific capacitance values of the device are shown in Fig. 8 (c) and were calculated according to Eq. S6. The specific capacitance of the constructed supercapacitor was found to be 88 F g^{-1} at 0.5 A g^{-1}, with a residual capacitance of about 72% confirming the fast ion transport as suggested by the CV curves. Fig. 8 (d) displays the Ragone plot of the symmetric cell exhibiting a charge storage performance with the remarkable specific energy of 32 Wh kg^{-1} at a specific power of 401 W kg^{-1} at 0.5 A g^{-1} which were calculated from Eqs. S6 and S7. Additionally, even at a high specific current of 10 A g^{-1}, the specific energy remained at 22 Wh kg^{-1} demonstrating a good rate capability. The symmetric device AC-PVA/PVP/Co-1//AC-PVA/PVP/Co-1 displays better electrochemical performance than many other similar devices such as Co-GPC//Co-GPC [16], Co_2@3D-CNF_S//NGH [54], NiCoP/NF//N-rGO/NF [55], Co_2P@N&P-CNF_S//CNF_S [56], SPC-F-$Co_{0.6}$// SPC-F-$Co_{0.6}$ [57]. This achievement is credited to the interconnected porous structure of the cross-linked polymer PVA/PVP and also the enhanced pseudocapacitive behaviour and increased conductivity owing to the presence of cobalt.

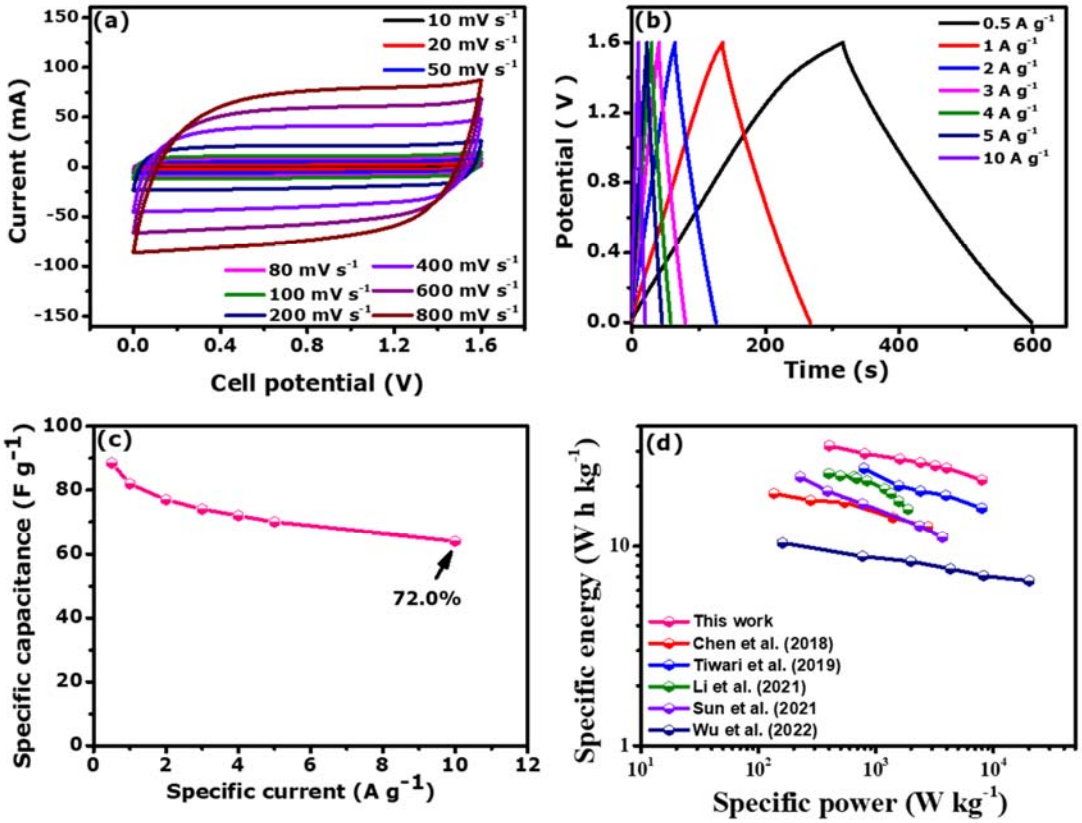

Fig. 8. (a) CV curves at different scan rates, (b) GCD curves at different specific currents, (c) specific capacitance against specific currents and (d) Ragone plot of the AC-PVA/PVP/Co-1//AC-PVA/PVP/Co-1 symmetric device.

Fig. 9 (a) displays the plot of capacitance retention and the Coulombic efficiency of the symmetric cell versus cycle number at a specific current of 5 A g^{-1}. The cycling stability over 10,000 cycles shows a capacitance retention of 91 % and a coulombic efficiency of 99.9 %. There is a slide decrease of the specific capacitance up to 3,000 cycles after that it became stable indicating a good cycling performance of the cell. Fig. 9 (b) depicts specific capacitance versus floating time, demonstrating an increase in specific capacitance at 5 A g^{-1} from 50 to 119 F g^{-1} after 190 h (8 days) floating time in an operating voltage of 1.6 V. The reduced capacitance during the first 30 hours might be due to the lack of wettability [58]. This behaviour was also observed in our previous studies [59]. This improvement was also visible in the GCD curves of Fig. 9 (c), which showed enhanced discharge time compared to the plots before and after stability. This improvement shows that, after 190 hours, the electrode pores are more accessible to the electrolyte ions [60]. The capacitance, specific energy, and power of the device before and after stability and also after voltage holding were estimated using the GCD curves displayed in Fig. 9 (c) using equations. S6 – S8, respectively and estimated values are displayed in Table 3. It can be seen that the device after voltage holding has increased performance as can be also seen by the increased charge-discharge time in Fig. 9 (c). The increase can be allotted to the availability of more pores during the voltage holding test i.e. the electrolyte is now being exposed to initially dormant porous storage sites which leads to an increase in the capacitance of the cell.

Table 3. Calculated device parameters at 5 A g^{-1}

Parameters	Before stability	After stability	After stability and voltage holding
Specific capacitance (F g^{-1})	69.4	58.4	120.7
Specific power (W kg^{-1})	4005.6	4004.2	4003.9
Specific energy (Wh kg^{-1})	24.7	20.8	42.9
Maximum power (kW kg-^{1})	298.5	204.1	400.0

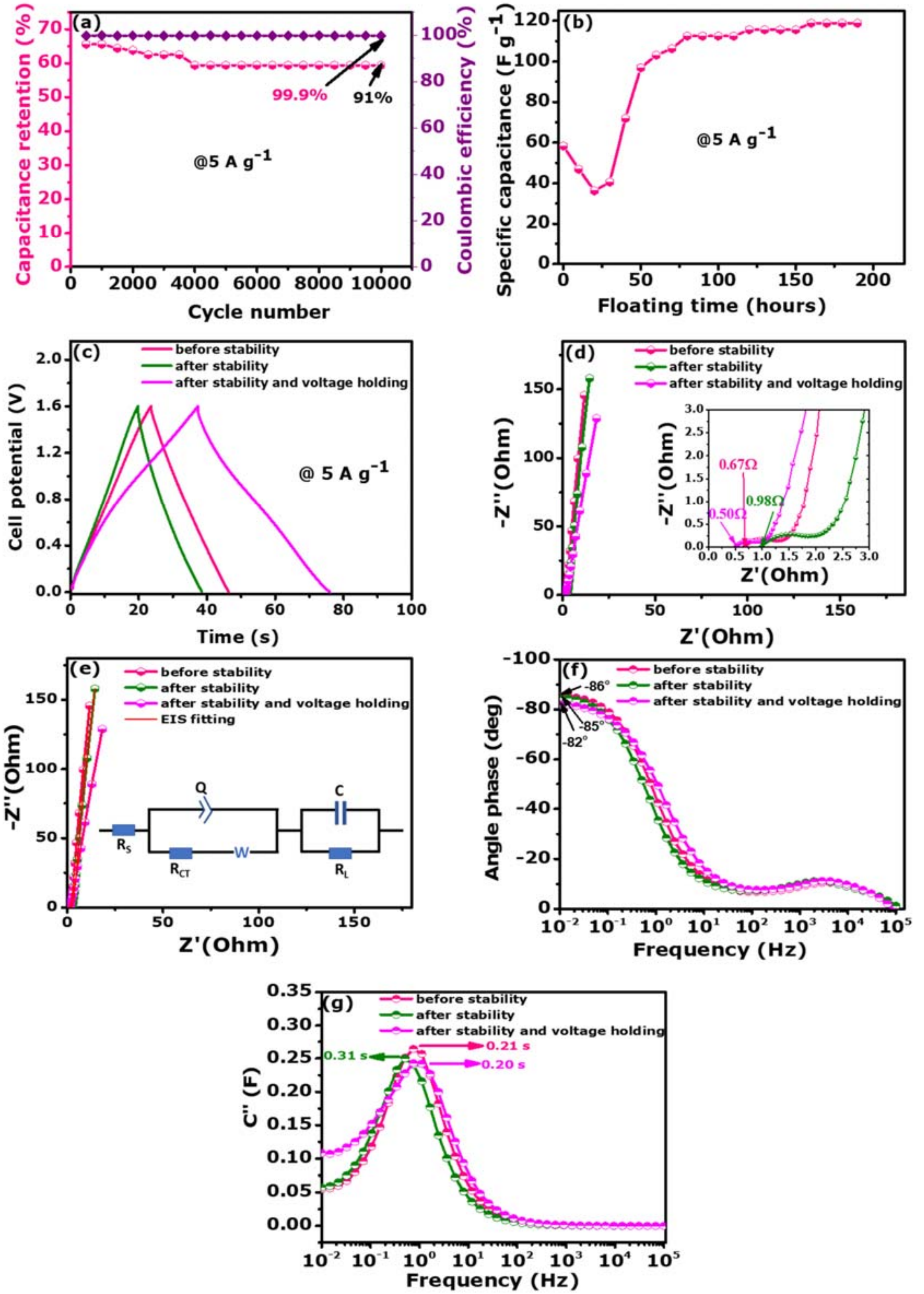
(a)
Capacitance retention (%)
Coulombic efficiency (%)
99.9%
91%
@5 A g^{-1}
Cycle number
(b)
Specific capacitance (F g^{-1})
@5 A g^{-1}
Floating time (hours)
(c)
before stability
after stability
after stability and voltage holding
Cell potential (V)
@ 5 A g^{-1}
Time (s)
(d)
before stability
after stability
after stability and voltage holding
-Z''(Ohm)
Z'(Ohm)
0.67Ω
0.98Ω
0.50Ω
(e)
before stability
after stability
after stability and voltage holding
EIS fitting
Q
C
R$_S$
R$_{CT}$
W
R$_L$
-Z''(Ohm)
Z'(Ohm)
(f)
before stability
after stability
after stability and voltage holding
-86°
-85°
-82°
Angle phase (deg)
Frequency (Hz)
(g)
before stability
after stability
after stability and voltage holding
0.31 s
0.21 s
0.20 s
C'' (F)
Frequency (Hz)

Fig. 9. (a) Columbic efficiency and specific capacitance retention against cycle number, (b) specific capacitance as function of voltage holding time up to 190 h, (c) GCD curves, (d) Nyquist plots, (e) EIS fitting, (f) phase angle, and (g) imaginary capacitance of the device before and after voltage holding for the AC-PVA/PVP/Co-1//AC-PVA/PVP/Co-1 symmetric device.

EIS Nyquist plot of the AC-PVA/PVP/Co-1//AC-PVA/PVP/Co-1 symmetric supercapacitor before and after stability and also after voltage holding is displayed in Fig. 9 (d). The values of the ESR before stability, after the 10,000 cycling and after the floating time are found to be 0.67, 0.98 and 0.5 Ω, respectively. After subjecting the device to 10,000 charge/discharge and 190 h floating time, a decrease in the diffusion length was observed. These results suggest a good diffusion and accessibility of the ions into the material. The maximum power, P_{max} of the devices was determined from the equation (1) below [61].

$$P_{max} = \frac{\Delta V^2}{4m(ESR)} \qquad \ldots (1)$$

where ΔV, m and ESR are the cell potential (V), total mass (of 4.2×10^{-6} kg) and ESR determined from the Nyquist plot in Fig. 9(d), respectively.

The EIS fitting of the plots displayed in Fig. 9 (d) and the used equivalent circuit are displayed in Fig. 9 (d) and (e) were generated via the ZFIT/EC-Lab version 11.33 using the Randomise + Simplex method. The fitting was obtained at the optimized minimization error i.e. chi-squared (χ2) and $\chi/\sqrt{N}$. The $\chi/\sqrt{N}$ is a normalized expression of χ2, where N is the number of data points, whose value is independent of the number of points. It can be seen from the Nyquist plot in Fig. 9 (d) and (e) that there is an insignificant difference between the three EIS spectra. Thus, one equivalent circuit fitted all the EIS spectra. In the equivalent circuit, the Rs is connected in series with a constant phase element Q, which is connected in parallel with the R_{CT} and Warburg diffusion element (W). The W which is responsible for the transition from high to low frequency is connected in series with R_{CT}. Ideally, at very low frequencies, an ideal polarizable capacitive electrode with the mass capacitance (C) should give rise to a straight line parallel to the imaginary axis. However, from the Nyquist plot in Fig. 9 (e), there is a divergence from this ideal capacitor behaviour. This divergence is attributed to the existence of a resistive element associated with C. This resistance is denoted as leakage resistance R_L which is in parallel to C.

The Phase angle values of the devices displayed in Fig. 9 (f) were observed to be above -80 degree which is very close to the ideal phase angle of -90 degrees and such behaviour was anticipated from the good CV and GCD curves. The frequency-dependent real $C'(\omega)$ and imaginary $C''(\omega)$ capacitance were calculated and displayed in Figs. S5 and 9(g) using the following equations 2-5 [61].

The impedance $Z(\omega)$ is expressed as

$$Z(\omega) = \frac{1}{j\omega \times C(\omega)} \qquad \ldots (2)$$

where $\omega = 2\pi f$. Therefore,

$$C'(\omega) = \frac{Z''(\omega)}{\omega |Z(\omega)|^2} \qquad \ldots (3)$$

$$C''(\omega) = \frac{Z'(\omega)}{\omega |Z(\omega)|^2} \qquad \ldots (4)$$

where $Z'(\omega)$ and $Z'(\omega)$ are defined as

$$|Z(\omega)|^2 = |Z'(\omega)|^2 + |Z''(\omega)|^2 \qquad \ldots (5)$$

Figs. S5 and 9(g) indicate that the cell after stability and voltage holding has the highest $C'(\omega)$ real accessible capacitance and the shortest relaxation time of 0.2s which suggest that the device holds more charge and can be charged in a few seconds. These attractive results demonstrate a potential application in supercapacitor energy-storage devices.

4. Conclusion

A Co-doped activated carbon from cross-linked PVA/PVP polymer (AC-PVA/PVP-Co-x (x= 0.5% w/v; 1% w/v; 2% w/v) was successfully synthesized using an easy single-way hydrothermal method by varying the amount of cobalt nitrate in PVA/PVP and followed by one-way KOH-activation, for the construction of a symmetric cell. It has been demonstrated that doping the cross-linked PVA/PVP polymers with certain quantities of cobalt has a significant impact on the prepared sample's capacitive behaviour and conductivity. At a specific current of 1 A g^{-1}, AC-PVA/PVP/Co-1 electrode had the highest specific capacitance (280 F g^{-1}) among all Co-doped ACs. AC-PVA/PVP/Co-1//AC-PVA/PVP/Co-1 symmetric supercapacitor exhibited a good electrochemical performance with a specific energy and specific power of 32 Wh kg^{-1} and 401 W kg^{-1}, respectively. These results lead to the conclusion that adding the appropriate amount of cobalt in the cross-linked PVA/PVP polymer under hydrothermal conditions yields a good electrode material for use in the field of energy storage.

Acknowledgements

This study is supported by the South African Research Chairs Initiative in Carbon Technology and Materials of the Department of Science and Technology and National Research Foundation of South Africa (Grant No. 61056). Any opinion, finding, and recommendation detailed in this work are those of the author(s), and the NRF is not liable in this regard. D. T. Bakhoum acknowledges the Organization for Women in Science for the Developing World (OWSD) and Swedish International Development Cooperation Agency (Sida) and the University of Pretoria for the financial support towards this research.

References

[1] T. Liu, L. Zhang, W. You, J. Yu, T. Liu, L. Zhang, W. You, J. Yu, Core–Shell Nitrogen-Doped Carbon Hollow Spheres/Co3O4 Nanosheets as Advanced Electrode for High-Performance Supercapacitor, Small. 14 (2018) 1702407. https://doi.org/10.1002/small.201702407.

[2] Z.J. Zhang, Q.C. Zheng, L. Sun, D. Xu, X.Y. Chen, Two-Dimensional Carbon Nanosheets for High-Performance Supercapacitors: Large-Scale Synthesis and Codoping with Nitrogen and Phosphorus, Ind Eng Chem Res. 56 (2017) 12344–12353. https://doi.org/10.1021/acs.iecr7b03022.

[3] S. Lv, L. Ma, X. Shen, H. Tong, Nitrogen and sulfur co-doped porous chitosan hydrogel-derived carbons for supercapacitors, Journal of Electroanalytical Chemistry. 907 (2022) 116060. https://doi.org/10.1016/j.jelechem.2022.116060.

[4] Y.J. Lee, S. Park, J.G. Seo, J.R. Yoon, J. Yi, I.K. Song, Nano-sized metal-doped carbon aerogel for pseudo-capacitive supercapacitor, Current Applied Physics. 11 (2011) 631–635. https://doi.org/10.1016/j.cap.2010.10.016.

[5] Y. Liu, Z. Ma, X. Chen, Y. Ying, W. Shi, In-situ generated NiCo2O4/CoP polyhedron with rich oxygen vacancies interpenetrating by P-doped carbon nanotubes for high performance supercapacitors, J Colloid Interface Sci. 608 (2022) 2246–2256. https://doi.org/10.1016/j.jcis.2021.10.099.

[6] N.F. Sylla, S. Sarr, N.M. Ndiaye, B.K. Mutuma, A. Seck, B.D. Ngom, M. Chaker, N. Manyala, Enhanced Electrochemical Behavior of Peanut-Shell Activated Carbon/Molybdenum Oxide/Molybdenum Carbide Ternary Composites, Nanomaterials. 11 (2021) 1056. https://doi.org/10.3390/nano11041056.

[7] S. Sarr, N.F. Sylla, D.T. Bakhoum, N.M. Ndiaye, D.J. Tarimo, V.M. Maphiri, B.D. Ngom, N. Manyala, Vanadium dioxide sulphur-doped reduced graphene oxide composite as novel electrode material for electrochemical capacitor, J Energy Storage. 55 (2022) 105666. https://doi.org/10.1016/j.est.2022.105666.

[8] M.R. Pallavolu, N. Gaddam, A.N. Banerjee, R.R. Nallapureddy, S.W. Joo, Superior energy-power performance of N-doped carbon nano-onions-based asymmetric and symmetric supercapacitor devices, Int J Energy Res. 46 (2022) 1234–1249. https://doi.org/10.1002/er.7242.

[9] K. Gunasekaran Govindarasu, R. Venkatesan, M. Eswaran, P. Arumugam, Simple and efficient CVD synthesis of graphitic P-doped 3D cubic ordered mesoporous carbon at low temperature with excellent supercapacitor performance, Advanced Powder Technology. 33 (2022) 103439. https://doi.org/10.1016/j.apt.2022.103439.

[10] G. Ma, G. Ning, Q. Wei, S-doped carbon materials: Synthesis, properties and applications, Carbon N Y. 195 (2022) 328–340. https://doi.org/10.1016/j.carbon.2022.03.043.

[11] B.H. Poornima, T. Vijayakumar, Hydrothermal synthesis of Boron -doped porous carbon from Azadirachta Indica wood for supercapacitor application, Inorg Chem Commun. 145 (2022) 109953. https://doi.org/10.1016/j.inoche.2022.109953.

[12] D.T. Bakhoum, N.F. Sylla, S. Sarr, V.M. Maphiri, N.M. Ndiaye, D.J. Tarimo, A. Seck, B.D. Ngom, M. Chaker, N. Manyala, Nitrogen-phosphorous co-doped porous carbon from cross-linked polymers for supercapacitor applications, J Energy Storage. 68 (2023) 107695. https://doi.org/10.1016/j.est.2023.107695.

[13] M. Moniruzzaman, Y. Anil Kumar, M.R. Pallavolu, H.M. Arbi, S. Alzahmi, I.M. Obaidat, Two-Dimensional Core-Shell Structure of Cobalt-Doped@MnO2 Nanosheets Grown on Nickel Foam as a Binder-Free Battery-Type Electrode for Supercapacitor Application, Nanomaterials. 12 (2022) 3187. https://doi.org/10.3390/nano12183187/s1.

[14] S. Li, J. Yang, H. Wang, L. Chen, A High Yield and Cost-Effective Pathway for the Production of Iron Doped Porous Carbon Derived from Squid Pen as Supercapacitor Electrode Material, Waste Biomass Valorization. 14 (2023) 2815–2824. https://doi.org/10.1007/s12649-023-02063-1.

[15] P. Ramakrishnan, S. Shanmugam, Electrochemical Performance of Carbon Nanorods with Embedded Cobalt Metal Nanoparticles as an Electrode Material for Electrochemical Capacitors, Electrochim Acta. 125 (2014) 232–240. https://doi.org/10.1016/j.electacta.2014.01.103.

[16] Y. Chen, F. Liu, F. Qiu, C. Lu, J. Kang, D. Zhao, S. Han, X. Zhuang, Cobalt-doped porous carbon nanosheets derived from 2D hypercrosslinked polymer with CoN4 for high performance electrochemical capacitors, Polymers (Basel). 10 (2018) 1339. https://doi.org/10.3390/polym10121339.

[17] D.T. Bakhoum, K.O. Oyedotun, S. Sarr, N.F. Sylla, V.M. Maphiri, N.M. Ndiaye, B.D. Ngom, N. Manyala, A study of porous carbon structures derived from composite of cross-linked polymers and reduced graphene oxide for supercapacitor applications, J Energy Storage. 51 (2022) 104476. https://doi.org/10.1016/j.est.2022.104476.

[18] B. Tiwari, A. Joshi, M. Munjal, G. Kaur, R.K. Sharma, G. Singh, Synergistic combination of N/P dual-doped activated carbon with redox-active electrolyte for high performance supercapacitors, Journal of Physics and Chemistry of Solids. 161 (2022) 110449. https://doi.org/10.1016/j.jpcs.2021.110449.

[19] A. Sivakumar, S.S. Jude Dhas, T. Pazhanivel, A.I. Almansour, R.S. Kumar, N. Arumugam, C.J. Raj, S.A.M.B. Dhas, Phase Transformation of Amorphous to Crystalline of Multiwall Carbon Nanotubes by Shock Waves, Cryst Growth Des. 21 (2021) 1617–1624. https://doi.org/10.1021/acs.cgd.0c01464.

[20] S.M. Jadhav, R.S. Kalubarme, N. Suzuki, C. Terashima, J. Mun, B.B. Kale, S.W. Gosavi, A. Fujishima, Cobalt-Doped Manganese Dioxide Hierarchical Nanostructures for Enhancing Pseudocapacitive Properties, ACS Omega. 6 (2021) 5717–5729. https://doi.org/10.1021/acsomega.0c06150.

[21] Y. Ren, P. Ye, J. Chen, H. Wang, J. Ning, J. Shen, Y. Zhong, Y. Hu, Fabrication of copper-cobalt heterostructures confined inside N-doped carbon nanocages for long-lasting Zn-air batteries, J Power Sources. 545 (2022) 231908. https://doi.org/10.1016/j.jpowsour.2022.231908.

[22] J. Yuan, B. Li, C. Hao, Study on cobalt doped tin-based perovskite material with enhanced air stability, Mater Sci Semicond Process. 57 (2017) 95–98. https://doi.org/10.1016/j.mssp.2016.09.029.

[23] P. Hu, M. Long, X. Bai, C. Wang, C. Cai, J. Fu, B. Zhou, Y. Zhou, Monolithic cobalt-doped carbon aerogel for efficient catalytic activation of peroxymonosulfate in water, J Hazard Mater. 332 (2017) 195–204. https://doi.org/10.1016/j.jhazmat.2017.03.010.

[24] P.W. Chen, K. Li, Y.X. Yu, W. De Zhang, Cobalt-doped graphitic carbon nitride photocatalysts with high activity for hydrogen evolution, Appl Surf Sci. 392 (2017) 608–615. https://doi.org/10.1016/j.apsusc.2016.09.086.

[25] X. Zhou, B. Zhao, H. Lv, Low-dimensional cobalt doped carbon composite towards wideband electromagnetic dissipation, Nano Research 2022. 9 (2022) 1–10. https://doi.org/10.1007/s12274-022-4950-x.

[26] H. Jin, H. Zhou, P. Ji, C. Zhang, J. Luo, W. Zeng, C. Hu, D. He, S. Mu, ZIF-8/LiFePO4 derived Fe-N-P Co-doped carbon nanotube encapsulated Fe2P nanoparticles for efficient oxygen reduction and Zn-air batteries, Nano Research 2020 13:3. 13 (2020) 818–823. https://doi.org/10.1007/s12274-020-2702-3.

[27] Y. Hou, Z. Wen, S. Cui, S. Ci, S. Mao, J. Chen, An Advanced Nitrogen-Doped Graphene/Cobalt-Embedded Porous Carbon Polyhedron Hybrid for Efficient Catalysis of Oxygen Reduction and Water Splitting, Adv Funct Mater. 25 (2015) 872–882. https://doi.org/10.1002/adfm.201403657.

[28] H. Bi, X. He, H. Zhang, H. Li, N. Xiao, J. Qiu, N, P co-doped hierarchical porous carbon from rapeseed cake with enhanced supercapacitance, Renew Energy. 170 (2021) 188–196. https://doi.org/10.1016/j.renene.2021.01.099.

[29] Y. Zhang, L. Tao, C. Xie, D. Wang, Y. Zou, R. Chen, Y. Wang, C. Jia, S. Wang, Y. Zhang, L. Tao, C. Xie, D. Wang, Y. Zou, R. Chen, Y. Wang, S. Wang, C. Jia, Defect Engineering on Electrode Materials for Rechargeable Batteries, Advanced Ma. 32 (2020) 1905923. https://doi.org/10.1002/adma.201905923.

[30] X. Zhang, Y. Wang, X. Yu, J. Tu, D. Ruan, Z. Qiao, High-performance discarded separator-based activated carbon for the application of supercapacitors, J Energy Storage. 44 (2021) 103378. https://doi.org/10.1016/j.est.2021.103378.

[31] X. Wang, X. Fan, H. Lin, H. Fu, T. Wang, J. Zheng, X. Li, An efficient Co-N-C oxygen reduction catalyst with highly dispersed Co sites derived from a ZnCo bimetallic zeolitic imidazolate framework, RSC Adv. 6 (2016) 37965–37973. https://doi.org/10.1039/c6ra04771h.

[32] H. Karimi-Maleh, C. Karaman, O. Karaman, F. Karimi, Y. Vasseghian, L. Fu, M. Baghayeri, J. Rouhi, P. Senthil Kumar, P.L. Show, S. Rajendran, A.L. Sanati, A. Mirabi, Nanochemistry approach for the fabrication of Fe and N co-decorated biomass-derived activated carbon frameworks: a promising oxygen reduction reaction electrocatalyst in neutral media, J Nanostructure Chem. 12 (2022) 429–439. https://doi.org/10.1007/s40097-022-00492-3.

[33] B. Devi, A. Jain, B. Roy, B. Rao R, N.R. Tummuru, A. Halder, R.R. Koner, Cobalt-Embedded N-Doped Carbon Nanostructures for Oxygen Reduction and Supercapacitor Applications, ACS Appl Nano Mater. 3 (2020) 6354–6366. https://doi.org/10.1021/acsanm.0c00732.

[34] R. Hossain, R.K. Nekouei, I. Mansuri, V. Sahajwalla, In-situ O/N-heteroatom enriched activated carbon by sustainable thermal transformation of waste coffee grounds for supercapacitor material, J Energy Storage. 33 (2021) 102113. https://doi.org/10.1016/j.est.2020.102113.

[35] S.C. Hu, J. Cheng, W.P. Wang, G.T. Sun, L. Le Hu, M.Q. Zhu, X.H. Huang, Structural changes and electrochemical properties of lacquer wood activated carbon prepared by phosphoric acid-chemical activation for supercapacitor applications, Renew Energy. 177 (2021) 82–94. https://doi.org/10.1016/j.renene.2021.05.113.

[36] D. Duan, S. Zhong, J. Huo, J. Chen, X. Shi, H. Peng, X. Li, S. Liao, High-performance atomic Co/N co–doped porous carbon catalysts derived from Co–doped metal–organic frameworks for oxygen reduction, J Colloid Interface Sci. 634 (2023) 940–948. https://doi.org/10.1016/j.jcis.2022.12.102.

[37] J. Cui, X. Wang, L. Huang, C. Zhang, Y. Yuan, Y. Li, Environmentally friendly bark-derived Co-Doped porous carbon composites for microwave absorption, Carbon N Y. 187 (2022) 115–125. https://doi.org/10.1016/j.carbon.2021.10.077.

[38] J. He, Y. Chen, W. Lv, K. Wen, C. Xu, W. Zhang, Y. Li, W. Qin, W. He, From Metal-Organic Framework to Li2S@C-Co-N Nanoporous Architecture: A High-Capacity Cathode for Lithium-Sulfur Batteries, ACS Nano. 10 (2016) 10981–10987. https://doi.org/10.1021/acsnano.6b05696.

[39] R. Wang, J. Yang, X. Chen, Y. Zhao, W. Zhao, G. Qian, S. Li, Y. Xiao, H. Chen, Y. Ye, G. Zhou, F. Pan, Highly Dispersed Cobalt Clusters in Nitrogen-Doped Porous Carbon Enable Multiple Effects for High-Performance Li–S Battery, Adv Energy Mater. 10 (2020) 1–10. https://doi.org/10.1002/aenm.201903550.

[40] W. Qian, Y. Tan, Y. Yu, L. Zhang, X. Wu, B. Xue, Cobalt and nitrogen co-doping of porous carbon nanosphere as highly effective catalysts for oxygen reduction reaction and Zn-air battery, J Alloys Compd. 918 (2022) 165741. https://doi.org/10.1016/j.jallcom.2022.165741.

[41] L. Zhou, J. Meng, P. Li, Z. Tao, L. Mai, J. Chen, Ultrasmall cobalt nanoparticles supported on nitrogen-doped porous carbon nanowires for hydrogen evolution from ammonia borane, Mater Horiz. 4 (2017) 268–273. https://doi.org/10.1039/c6mh00534a.

[42] F. Guo, H. Yang, B. Aguila, A.M. Al-Enizi, A. Nafady, M. Singh, V. Bansal, S. Ma, Cobalt nanoparticles incorporated into hollow doped porous carbon capsules as a highly efficient oxygen reduction electrocatalyst, Catal Sci Technol. 8 (2018) 5244–5250. https://doi.org/10.1039/c8cy01371c.

[43] Y. Liu, Z. Chen, N. Zhao, G. Tong, Z. Li, B. Wang, Y. Du, Q. Pan, Z. Li, Y. Xie, Y. Yang, Ultra-small cobalt nanoparticles embedded into N-doped hierarchical porous

carbon derived from Ion-Exchange MOFs as high-efficient bifunctional catalysts for rechargeable Zn-air battery, Chemical Engineering Journal. 433 (2022) 134469. https://doi.org/10.1016/j.cej.2021.134469.

[44] N. Deng, H. Gao, G. Wang, L. Zhang, Cobalt-doped porous carbon nanofibers with three- dimensional network structures as electrocatalysts for enhancing oxygen reduction reaction, Int J Hydrogen Energy. (2023) 1–12. https://doi.org/10.1016/j.ijhydene.2023.01.262.

[45] Y. Zhang, L. Lu, S. Zhang, Z. Lv, D. Yang, J. Liu, Y. Chen, X. Tian, H. Jin, W. Song, Biomass chitosan derived cobalt/nitrogen doped carbon nanotubes for the electrocatalytic oxygen reduction reaction, J Mater Chem A Mater. 6 (2018) 5740–5745. https://doi.org/10.1039/c7ta11258k.

[46] Y. Yang, L. Jia, B. Hou, D. Li, J. Wang, Y. Sun, The effect of nitrogen on the autoreduction of cobalt nanoparticles supported on nitrogen-doped ordered mesoporous carbon for the fischer-tropsch synthesis, ChemCatChem. 6 (2014) 319–327. https://doi.org/10.1002/cctc.201300897.

[47] X. Shi, Z. Xu, C. Han, R. Shi, X. Wu, B. Lu, J. Zhou, S. Liang, Highly Dispersed Cobalt Nanoparticles Embedded in Nitrogen-Doped Graphitized Carbon for Fast and Durable Potassium Storage, Nanomicro Lett. 13 (2021) 21. https://doi.org/10.1007/s40820-020-00534-x.

[48] J.M. Yan, X.B. Zhang, H. Shioyama, Q. Xu, Room temperature hydrolytic dehydrogenation of ammonia borane catalyzed by Co nanoparticles, J Power Sources. 195 (2010) 1091–1094. https://doi.org/10.1016/j.jpowsour.2009.08.067.

[49] X. Zhang, L. Wu, Polyvinyl pyrrolidone regulated Co , N co - doped porous carbon for oxygen reduction reaction, Ionics (Kiel). 28 (2022) 3435–3443. https://doi.org/10.1007/s11581-022-04581-9.

[50] G. Kim, B.H. Kim, One-dimensional hierarchical porous carbon nanofibers with cobalt oxide in a hollow channel for electrochemical applications, J Alloys Compd. 910 (2022) 164886. https://doi.org/10.1016/j.jallcom.2022.164886.

[51] T.S. Mathis, N. Kurra, X. Wang, D. Pinto, P. Simon, Y. Gogotsi, Energy Storage Data Reporting in Perspective—Guidelines for Interpreting the Performance of Electrochemical Energy Storage Systems, Adv Energy Mater. 9 (2019) 1902007. https://doi.org/10.1002/aenm.201902007.

[52] S. Ashok C, A. Vazhayil, J. Thomas, N. Thomas, Enhanced electrochemical performance of facilely synthesized cobalt doped cubic NiO nanoflakes for supercapacitor application, J Energy Storage. 55 (2022) 105498. https://doi.org/10.1016/j.est.2022.105498.

[53] A. Moyseowicz, Z. González, R. Menéndez, G. Gryglewicz, Three-dimensional poly(aniline-co-pyrrole)/thermally reduced graphene oxide composite as a binder-free electrode for high-performance supercapacitors, Compos B Eng. 145 (2018) 232–239. https://doi.org/10.1016/j.compositesb.2018.03.018.

[54] A.P. Tiwari, S.H. Chae, G.P. Ojha, B. Dahal, T. Mukhiya, M. Lee, K. Chhetri, T. Kim, H.Y. Kim, Three-dimensional porous carbonaceous network with in-situ entrapped metallic cobalt for supercapacitor application, J Colloid Interface Sci. 553 (2019) 622–630. https://doi.org/10.1016/j.jcis.2019.06.070.

[55] P.P. Li, Y. Han, F. Yan, L. Yan, H. Huang, W. Zhou, Engineering NiCoP arrays by cross-linked nanowires and nanosheets as advanced materials for hybrid supercapacitors, J Energy Storage. 38 (2021) 102503. https://doi.org/10.1016/j.est.2021.102503.

[56] X. Sun, H. Liu, G. Xu, J. Bai, C. Li, Embedding Co2P nanoparticles into N&P co-doped carbon fibers for hydrogen evolution reaction and supercapacitor, Int J Hydrogen Energy. 46 (2021) 1560–1568. https://doi.org/10.1016/j.ijhydene.2020.10.018.

[57] S. Wu, C. Feng, B. Fan, Y. Li, H. Wang, Y. Zhou, N/O/P co-doped hierarchical porous graphitic carbon materials for high-rate supercapacitors, J Alloys Compd. 899 (2022) 163282. https://doi.org/10.1016/j.jallcom.2021.163282.

[58] P. Murovhi, D.J. Tarimo, K.O. Oyedotun, N. Manyala, High specific energy asymmetric supercapacitor based on alpha-manganese dioxide/activated expanded graphite composite and activated carbon-polyvinyl alcohol, J Energy Storage. 32 (2020) 101797. https://doi.org/10.1016/j.est.2020.101797.

[59] X. Li, Z. Lv, M. Wu, X. Li, Z. Li, N, P co-doped porous carbon from cross-linking cyclophosphazene for high-performance supercapacitors, Journal of Electroanalytical Chemistry. 881 (2021) 114952. https://doi.org/10.1016/j.jelechem.2020.114952.

[60] O. Fasakin, J.K. Dangbegnon, D.Y. Momodu, M.J. Madito, K.O. Oyedotun, M.A. Eleruja, N. Manyala, Synthesis and characterization of porous carbon derived from activated banana peels with hierarchical porosity for improved electrochemical performance, Electrochim Acta. 262 (2018) 187–196. https://doi.org/10.1016/j.electacta.2018.01.028.

[61] V.M. Maphiri, D.T. Bakhoum, S. Sarr, N.F. Sylla, G. Rutavi, N. Manyala, Low temperature thermally reduced graphene oxide directly on Ni-Foam using atmospheric pressure-chemical vapour deposition for high performance supercapacitor application, J Energy Storage. 52 (2022) 104967. https://doi.org/10.1016/j.est.2022.104967.